Chemistry–A European Journal
Research Article
doi.org/10.1002/chem.202200288
Chemistry Europe
European Chemical Societies Publishing
www.chemeurj.org

Boosting Hydrogen Evolution at Visible Light Wavelengths by Using a Photocathode with Modal Strong Coupling between Plasmons and a Fabry-Pérot Nanocavity

Tomoya Oshikiri,[a] Haruki Jo,[a] Xu Shi,[b] and Hiroaki Misawa*[a, c]

Abstract: Hot-hole injection from plasmonic metal nanoparticles to the valence band of p-type semiconductors and reduction by hot electrons should be improved for efficient and tuneable reduction to obtain beneficial chemical compounds. We employed the concept of modal strong coupling between plasmons and a Fabry-Pérot (FP) nanocavity to enhance the hot-hole injection efficiency. We fabricated a photocathode composed of gold nanoparticles (Au–NPs), p-type nickel oxide (NiO), and a platinum film (Pt film) (ANP). The ANP structure absorbs visible light over a broad wavelength range from 500 nm to 850 nm via hybrid modes based on the modal strong coupling between the plasmons of Au–NPs and the FP nanocavity of NiO on a Pt film. All wavelength regions of the hybrid modes of the modal strong coupling system promoted hot-hole injection from the Au–NPs to NiO and proton/water reduction by hot electrons. The incident photon-to-current efficiency based on H_2 evolution through water/proton reduction by hot electrons reached 0.2% at 650 nm and 0.04% at 800 nm.

Introduction

Hot electron and hole pairs generated via nonradiative decay of localized surface plasmon resonances (LSPRs) attract considerable attention for triggering chemical reactions.[1] The hot-electron injection from plasmonic metals to the conduction band of n-type semiconductors and subsequent oxidation have been widely studied.[2] Additionally, the remaining holes have been reported to have the ability to oxidize water.[3] Recently, we reported that the light absorption and water oxidation ability were dramatically enhanced by modal strong coupling between LSPR and a Fabry-Pérot (FP) nanocavity.[4] We found that the coupling strength, that is, the energy exchange rate between two original modes, affects the photoelectrochemical performance under modal strong coupling conditions.[5]

In the photoanode with a combination of a metal and an n-type semiconductor, reduction is performed by the electrons injected into the conduction band of the semiconductor. Therefore, the reduction potential is restricted by the band structure of the semiconductor, and the additional energy of the LSPR used for hot-electron excitation is lost (Figure 1a). In contrast, the photocathode composed of a plasmonic metal and a hole-trapping material effectively induces reduction because hot electrons reduce the substances, which involves hot-hole injection from the metal to the hole-trapping material (Figure 1b). Furthermore, Atwater et al. reported that hot-hole injection from gold to a p-type semiconductor is thermodynamically preferable to hot-electron injection from gold to an n-type semiconductor due to the energy distribution of hot carriers generated in gold estimated by theoretical calculations.[6] Recently, plasmonic photocathodes have been investigated to perform reduction.[7] However, the plasmonic

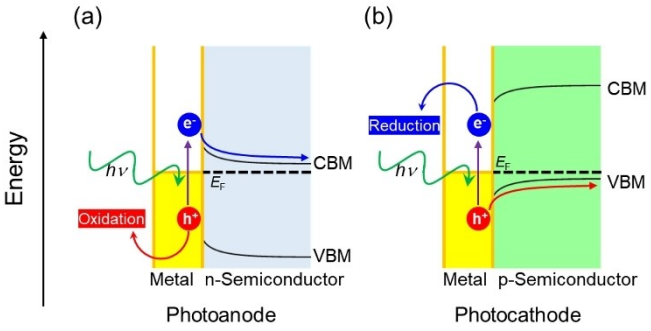

Figure 1. a) Hot-electron injection at the interface of a plasmonic metal and an n-type semiconductor. b) Hot-hole injection at the interface of a plasmonic metal and a p-type semiconductor. CBM, VBM, and E_F indicate the conduction band minimum, valence band maximum, and Fermi level, respectively.

[a] *Dr. T. Oshikiri, H. Jo, Prof. H. Misawa*
Research Institute for Electronic Science
Hokkaido University
N21W10, Kita-ku, Sapporo, 001-0021 (Japan)
E-mail: misawa@es.hokudai.ac.jp
[b] *Dr. X. Shi*
Creative Research Institution
Hokkaido University
N21W10, Kita-ku, Sapporo 001-0021 (Japan)
[c] *Prof. H. Misawa*
Center for Emergent Functional Matter Science
National Yang Ming Chiao Tung University
Hsinchu, 30010 (Taiwan)

Supporting information for this article is available on the WWW under https://doi.org/10.1002/chem.202200288

photocathode using a single layer of metallic nanoparticles has the same problem as the anode. The absorptivity is not sufficient, and consequently, the photoelectrochemical reaction efficiency is limited. We assume that the strong coupling between the LSPR and a FP nanocavity also enhances the absorption and reaction efficiencies on the photocathode. The aim of this study is to experimentally verify whether modal strong coupling enhances hot-hole injection from the metal nanoparticle to the p-type semiconductor. We employed gold nanoparticles (Au–NPs) as a plasmonic metal, lithium-doped nickel oxide (NiO) as a p-type semiconductor, and a platinum film (Pt film) as a reflection layer. A dielectric film with a high refractive index on a metallic film, such as NiO on a Pt film, works as an FP nanocavity.[8] Additionally, Pt film has enough resistance against thermal deformation during the annealing process.

Results and Discussion

Au–NP/NiO/Pt-film (ANP, Figures 2a and b) structures were fabricated as follows. We employed a pulsed laser deposition (PLD) procedure to precisely control the deposition thickness of NiO. First, a Pt film with a thickness of 100 nm was sputtered on a yttrium-stabilized zirconium oxide (YSZ) substrate. Then, a NiO layer was deposited by PLD at 25 °C. After that, an Au film with a thickness of 3 nm was evaporated. Finally, the substrate was annealed at 900 °C to form Au–NPs and increase the crystallinity of NiO. From the X-ray diffraction (XRD) pattern, the (111) orientation of the NiO crystal on Pt (111) and YSZ (111) was clearly observed (Figure S1a).

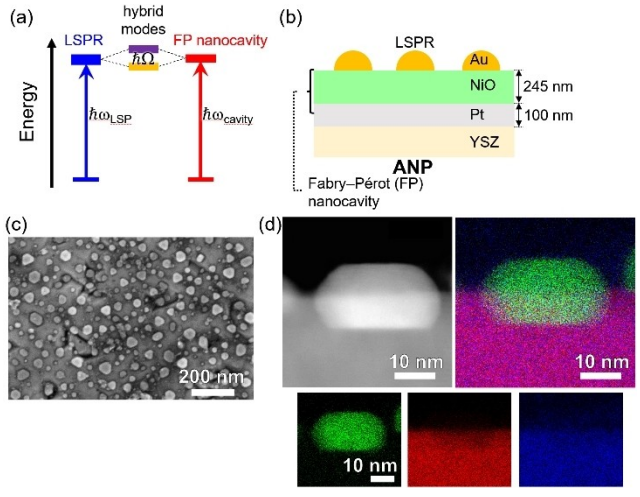

Figure 2. a) Energy-level diagram of the modal strong coupling between the LSPR and FP nanocavity modes. Ω, ω_{LSP}, and ω_{cavity} are the splitting frequency of modal strong coupling and resonant frequencies of the LSPR and FP nanocavity modes. b) Schematic of the ANP structure. c) Top-view SEM image of the ANP structure. (d) Cross-section of a Au–NP inlaid in a NiO layer. Left: high-angle annular dark field (HAADF)-STEM image; right: energy-dispersive X-ray spectrometry (EDS) mapping. The green, red and blue colours depict Au, Ni and O elements, respectively. The lower panels show EDS mapping of each element.

The NiO atoms were speculated to be aligned along the crystalline lattice of the Pt film based on the deposition mechanism of PLD. Figure 2c shows the surface morphology of the ANP structure measured by scanning electron microscopy (SEM). The formation of Au–NPs was observed, and the average particle diameter and the standard deviation were 39 and 14 nm, respectively. The detailed analysis is shown in Figure S1b. The cross-section of the structure was investigated by scanning transmission electron microscopy (STEM). Dense and flat films of Pt and NiO were observed, as shown in Figures S1c and S1d. The lattice structures of NiO and Au–NPs were clearly observed, indicating good crystallinity (Figure S1e). The interplanar distance of the NiO crystal was estimated to be 2.4 ± 0.2 Å, corresponding to the interplanar distance of NiO in the (111) direction, as expected from the XRD result.[9] The interplanar distance of Au–NPs was close to that of the NiO crystal, indicating Au (111).[10] Interestingly, some Au–NPs were partially or fully inlaid in the NiO layer even though they were self-organized by simple annealing of the Au thin film (Figure 2d). This is due to the lattice matching of Au and NiO.[11] The partial inlaying of Au–NPs plays a critical role in forming a three-phase interface of Au/NiO/substance for chemical reactions in addition to increasing the modal strong coupling strength.[4,12] To form the strong coupling between the LSPR and FP nanocavity, a large spatial overlap of LSPR and cavity modes is required. Figure S2 clearly indicates that the splitting of upper and lower branches became obvious as an increase of the inlaid depth. On the other hand, full coverage of Au–NPs by the NiO layer prevents the reduction of substances near the strong electric field.

The diameter of Au–NPs fabricated by this study is approximately 40 nm, which is 1.5 to three times larger than those of previous works on modal strong coupling between LSPR and a FP nanocavity.[4–5] Larger metallic NPs have been reported to interact with a metallic mirror through a thin insulator.[13] The electric field distribution and vector of the ANP structure with a NiO layer thickness of 40 nm showed that the electric field of the LSPR of Au–NPs reached the Pt surface, perturbing the reflected light field on Pt (Figure S3a). This inhomogeneous light reflection induces complex optical modes and disturbs the understanding of the effect of the strong coupling between a pure FP nanocavity and the LSPR. In contrast, the LSPR of Au–NPs did not affect the Pt film when the NiO layer thickness was 240 nm (Figure S3b). Therefore, to evaluate the modal coupling between the LSPR of Au–NPs and FP nanocavity of NiO on a Pt film, we employed a second-order FP nanocavity using a thicker NiO layer. First, finite-difference time-domain (FDTD) simulations were performed to confirm the modal coupling using a second-order FP nanocavity (Figure 3a). We focused on the average diameter of 40 nm for the calculations. Half of the Au–NPs are distributed from 30 to 50 nm based on the analysis of Figure S1b. Therefore, the coverage ratio of the simulation was set to 6.9 %, which is half the total coverage by all Au–NPs. From the absorption spectra shown in Figure 3b, two peaks derived from energy-level splitting into upper and lower branches are observed. Figure 3c shows a dispersion curve obtained by plotting the peak energy

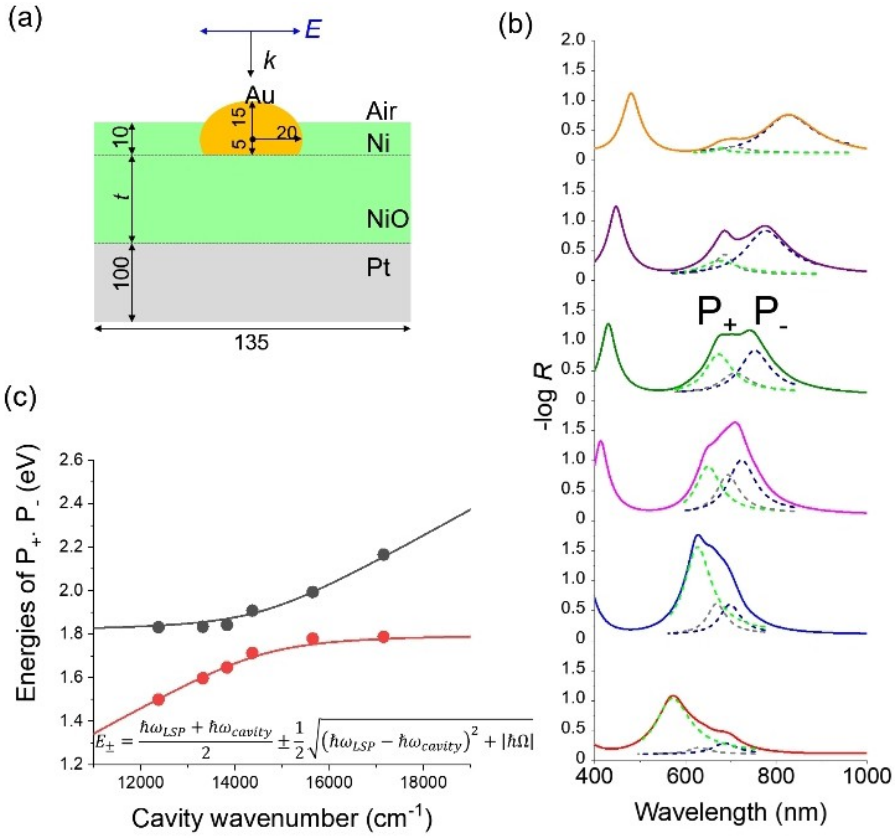

Figure 3. a) Cross-sectional view of the geometric model for FDTD simulations. Numbers indicate lengths in nm. The variable *t* indicates the NiO thickness excluding the inlay depth of 10 nm. b) Absorption spectra of ANP structures with different thicknesses of NiO obtained by FDTD simulations. *R* indicates the reflectance. The transmittance *T* was negligibly small because the ANP structures included Pt films with thicknesses of 100 nm. The *t* values were 180 nm (red), 200 nm (blue), 220 nm (magenta), 230 nm (green), 240 nm (purple), and 260 nm (orange). The broken curves in light green and navy indicate the Lorentz fitting of the absorption band of the upper and lower branches (P_+, P_-). The grey curves indicate the uncoupled mode. c) Dispersion curve of the absorption band shown in panel b). The black and red curves are fittings obtained using a coupled harmonic oscillator model. $E_\pm$ indicates the energy of P_+ and P_-.

of the upper and lower branches as a function of the wavenumber of the cavity resonances of NiO on a Pt film with various NiO thicknesses. The splitting energy was calculated to be 200 meV using a coupled harmonic oscillator model.[4,14] In the strong coupling regime, the frequency Ω of the coupled system is higher than the dephasing time of both oscillators.[15] In other words, the two absorption bands derived from hybrid states should fulfil Equation (1).

$$\hbar\Omega > \sqrt{\frac{\gamma_{UB}^2}{2} + \frac{\gamma_{LB}^2}{2}} = \sqrt{\frac{\gamma_{cavity}^2}{2} + \frac{\gamma_{LSPR}^2}{2}} \quad (1)$$

where $\hbar\Omega$ is the splitting energy, γ_{UB} and γ_{LB} are the linewidths of the upper and lower branch modes when the energies of the nanocavity and LSPR modes are equal, and γ_{cavity} and γ_{LSPR} are the linewidths of the nanocavity and LSPR modes, respectively. Here, the root mean square (RMS) of γ_{UB} and γ_{LB} represented by the centre part in Equation (1) was estimated to be 180 meV, which is smaller than the splitting energy of 200 meV. Therefore, the ANP structure can fulfil the strong coupling condition in principle. Based on the FDTD simulations, we fabricated an ANP structure with a NiO thickness of 245 nm and an FP cavity wavenumber of 15100 cm^{-1}, which is close to the tuning condition calculated from Figure 3c (14600 cm^{-1}). The absorption spectrum showed a broad absorption band, as shown in Figure 4. The two peaks derived from hybrid modes are not apparently distinguished due to the broadness of the LSPR mode derived from the inhomogeneities of the Au–NP

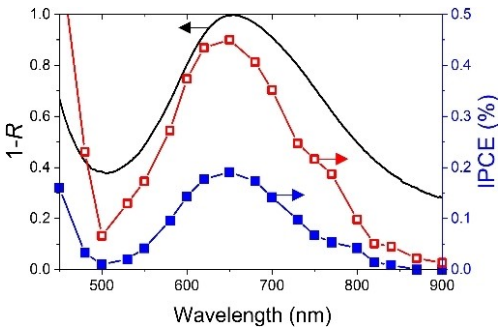

Figure 4. Absorption spectrum and IPCE action spectra of the ANP photocathode with a NiO thickness of 245 nm in an aqueous solution of 0.1 mol dm^{-3} $KClO_4$ with (red) and without (blue) 0.1 mol dm^{-3} $K_2S_2O_8$.

diameters and interparticle distances. For example, the different particle diameters of Au–NPs gave different peak splitting in the FDTD simulation. Additionally, the ANP structure with inhomogeneous diameters of Au–NPs, with a similar particle diameter distribution as the experimental result, showed a broad absorption band that could not be clearly divided into two bands (Figure S4). However, the ANP structure can form modal strong coupling, as discussed above. Importantly, more than 99% of light with a wavelength of 650 nm was absorbed by the ANP structure. The contribution of hybrid modes to the absorption was estimated to be 70% at 650 nm by subtracting the baseline derived from the absorption of the Pt film. This absorption efficiency is dramatically enhanced compared to the LSPR alone (Figure S5). Such significant absorption enhancement is derived from strong coupling rather than weak coupling.

We performed photoelectrochemical measurements to determine the photoreduction performance of the ANP photocathode using a conventional three-electrode system. First, current-potential (*I–V*) characteristics and Mott-Schottky plots were obtained in neutral 0.1 mol dm^{-3} $KClO_4$ aqueous solution. The rectification properties of a p-type semiconductor were observed from the *I–V* characteristics, indicating that the ANP works as the cathode (Figure S6a). Additionally, from the intercept and slope of the Mott-Schottky plot, the flat-band potential and the acceptor density were estimated to be 0.87 V vs. reversible hydrogen electrode (RHE) and 8.5×10^{19} cm^{-3}, respectively (Figure S6b). These values are consistent with the reported flat-band potential and acceptor density of NiO.[16] Figure 4 also shows the action spectra of the incident photon-to-current conversion efficiency (IPCE) of the ANP photocathode with and without potassium persulfate ($K_2S_2O_8$) as a sacrificial electron acceptor. Because $S_2O_8^{2-}$ is an excellent one-electron acceptor with fast reaction kinetics, the consumption of electrons generated in Au–NPs is accelerated. In the presence of $K_2S_2O_8$, obvious IPCE values were observed from 500 to 800 nm, and the maximum value reached 0.45% at 650 nm. Additionally, the shape of the action spectrum corresponds well to that of the absorption spectrum. Therefore, the broad IPCE action spectral band suggests that the hot holes excited by all wavelength regions of hybrid modes were injected from Au–NPs into NiO in the ANP photocathode, and the hot electrons reduce substances under modal strong coupling conditions. To discuss the apparent charge separation efficiency, the internal quantum efficiency (IQE) was obtained by dividing the IPCE value by the absorption in the presence of the sacrificial electron acceptor. Figure S7 depicts the IQE spectrum of the ANP photocathode. The averaged IQE for wavelengths from 550 to 800 nm was 0.72%. Surprisingly, the shape of the IPCE action spectrum excluding the sacrificial reagent did not change, although the absolute values became approximately half, as shown by the blue curve in Figure 4. In this case, water or protons act as electron acceptors. Therefore, photocurrent generation based on H_2 evolution via water/proton reduction by hot electrons is clearly observed even at 800 nm. The maximum value of the IPCE reached 0.2% at 650 nm, which was significantly larger than that of Au–NPs on NiO without a Pt film (Figure S4).

To obtain direct evidence of H_2 evolution by using water as an electron acceptor, we quantified the evolved H_2 under visible light irradiation (410–800 nm) by using the ANP photocathode as a working electrode of a three-electrode system. Under irradiation conditions, the amount of evolved H_2 gas from the ANP photocathode linearly increased, as shown in Figure 5a. The reaction rate of H_2 evolution was estimated to be 23 nmol cm^{-2} h^{-1}. Furthermore, a stable cathodic photocurrent was obtained for at least 9 h (Figure 5b). The Faradaic efficiency was approximately 70% for H_2 evolution when the irradiation time was 9 h. Additionally, the comparison to the conventional plasmonic photocathodes is summarized in Table S1. Because the total amount of Au atoms within the reaction area of ANP was roughly calculated to be 20 nmol cm^{-2}, the turnover number at a reaction time of 9 h was approximately 10, much larger than 1. These results indicate that the ANP photocathode works as a robust photocatalytic cathode for H_2 evolution under visible light irradiation.

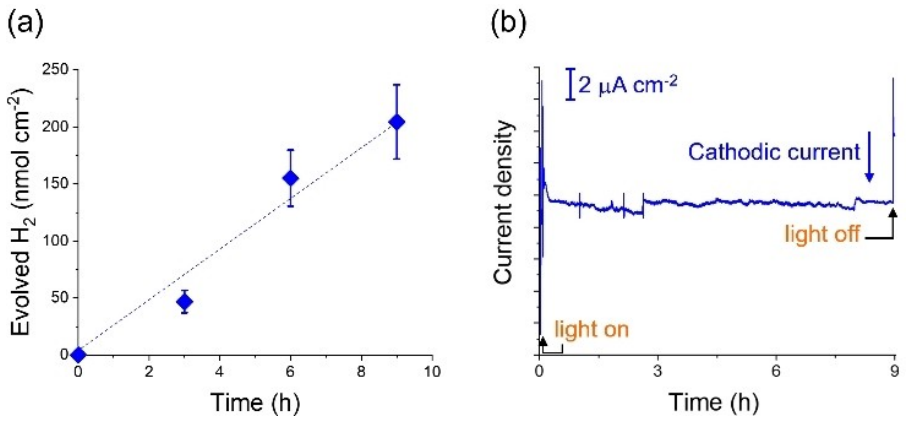

Figure 5. a) H_2 evolution on the ANP photocathode with a NiO thickness of 245 nm. Error bars indicate the standard deviations. b) Current density-time characteristics of the ANP cathode. Irradiation wavelengths were from 410 nm to 800 nm. The applied potential was −0.7 V vs. Pt quasi-reference electrode.

Conclusion

In conclusion, we fabricated a novel ANP photocathode by combining the LSPR of Au–NPs and the FP nanocavity of NiO on a Pt film. ANP absorbs visible light over a broad wavelength range via hybrid modes based on the modal strong coupling between the LSPR and FP nanocavity. Interestingly, Au–NPs were spontaneously inlaid in the NiO layer by high-temperature annealing due to the lattice matching between Au and NiO. The hybrid modes of the modal strong coupling system promoted hot-hole transfer from the Au NPs to NiO and H_2 evolution through water reduction by hot electrons. The water reduction system on ANP photocathodes worked up to 800 nm. Our investigation demonstrates that the concept of modal strong coupling can be applied to photocathodes for reduction of chemical compounds. The absorption efficiency and wavelength can be arbitrarily designed via modal strong coupling. Furthermore, several studies in addition to this study suggest that modal strong coupling enhances not only the absorptivity but also the hot-electron and -hole injection efficiencies from a metal to a semiconductor.[13] Modal strong coupling is expected to be applied for a wide variety of photochemical reactions to solve the issue of enhancing hot-carrier injection. Understanding the hot-electron and -hole transfer dynamics using time-resolved photoemission electron microscopy and transient absorption measurements pumped by an ultrashort pulse laser is important. In the near future, we will work on these studies.

Acknowledgements

We are grateful to Yuko Mori, Naomi Hirai, and Prof. Yasutaka Matsuo at Hokkaido University for STEM measurements. We are grateful to Prof. Hiromichi Ohta at Hokkaido University for helping PLD target fabrication. We acknowledge financial support from JSPS KAKENHI (Grant Nos. JP18H05205, JP20H05083, and JP20K15113), the Nanotechnology Platform (Hokkaido University), and the Dynamic Alliance for Open Innovation Bridging Human, Environment and Materials (Five-Star Alliance) of MEXT.

Conflict of Interest

The authors declare no conflict of interest.

Data Availability Statement

The data that support the findings of this study are available from the corresponding author upon reasonable request.

Keywords: artificial photosynthesis · hydrogen evolution · modal strong coupling · photocatalysis · surface plasmon resonance

[1] a) C. Sönnichsen, T. Franzl, T. Wilk, G. von Plessen, J. Feldmann, O. Wilson, P. Mulvaney, *Phys. Rev. Lett.* **2002**, *88*, 077402; b) M. L. Brongersma, N. J. Halas, P. Nordlander, *Nat. Nanotechnol.* **2015**, *10*, 25–34; c) J. G. Liu, H. Zhang, S. Link, P. Nordlander, *ACS Photonics* **2017**, *5*, 2584–2595; d) A. M. Brown, R. Sundararaman, P. Narang, W. A. Goddard 3rd, H. A. Atwater, *ACS Nano* **2016**, *10*, 957–966.
[2] a) G. Zhao, H. Kozuka, T. Yoko, *Thin Solid Films* **1996**, *277*, 147–154; b) Y. Tian, T. Tatsuma, *J. Am. Chem. Soc.* **2005**, *127*, 7632–7637; c) A. Furube, L. Du, K. Hara, R. Katoh, M. Tachiya, *J. Am. Chem. Soc.* **2007**, *129*, 14852–14853; d) D. B. Ingram, S. Linic, *J. Am. Chem. Soc.* **2011**, *133*, 5202–5205; e) C. Clavero, *Nat. Photonics* **2014**, *8*, 95–103; f) K. Wu, J. Chen, J. R. McBride, T. Lian, *Science* **2015**, *349*, 632–635; g) T. Oshikiri, K. Ueno, H. Misawa, *Angew. Chem. Int. Ed.* **2016**, *55*, 3942–3946; *Angew. Chem.* **2016**, *128*, 4010–4014; h) T. Oshikiri, K. Ueno, H. Misawa, *Green Chem.* **2019**, *21*, 4443–4448.
[3] a) Y. Nishijima, K. Ueno, Y. Kotake, K. Murakoshi, H. Inoue, H. Misawa, *J. Phys. Chem. Lett.* **2012**, *3*, 1248–1252; b) Y. Zhong, K. Ueno, Y. Mori, X. Shi, T. Oshikiri, K. Murakoshi, H. Inoue, H. Misawa, *Angew. Chem. Int. Ed.* **2014**, *53*, 10350–10354; *Angew. Chem.* **2014**, *126*, 10518–10522; c) S. Wang, Y. Gao, S. Miao, T. Liu, L. Mu, R. Li, F. Fan, C. Li, *J. Am. Chem. Soc.* **2017**, *139*, 11771–11778; d) M. Okazaki, Y. Suganami, N. Hirayama, H. Nakata, T. Oshikiri, T. Yokoi, H. Misawa, K. Maeda, *ACS Appl. Energ. Mater.* **2020**, *3*, 5142–5146; e) X. Shi, X. Li, T. Toda, T. Oshikiri, K. Ueno, K. Suzuki, K. Murakoshi, H. Misawa, *ACS Appl. Energ. Mater.* **2020**, *3*, 5675–5683.
[4] X. Shi, K. Ueno, T. Oshikiri, Q. Sun, K. Sasaki, H. Misawa, *Nat. Nanotechnol.* **2018**, *13*, 953–958.
[5] Y. Suganami, T. Oshikiri, X. Shi, H. Misawa, *Angew. Chem. Int. Ed.* **2021**, *60*, 18438–18442; *Angew. Chem.* **2021**, *133*, 18586–18590.
[6] J. S. DuChene, G. Tagliabue, A. J. Welch, W. H. Cheng, H. A. Atwater, *Nano Lett.* **2018**, *18*, 2545–2550.
[7] a) F. Zheng, L.-W. Wang, *J. Phys. Chem. Lett.* **2019**, *10*, 6174–6183; b) L. Zhang, X. Chen, Z. Hao, X. Chen, Y. Li, Y. Cui, C. Yuan, H. Ge, *ACS Appl. Mater. Interfaces* **2019**, *2*, 3654–3661; c) H. Robatjazi, S. M. Bahauddin, C. Doiron, I. Thomann, *Nano Lett.* **2015**, *15*, 6155–6161; d) D. Sato, H. Minamimoto, K. Murakoshi, *Chem. Lett.* **2020**, *49*, 806–808; e) G. Tagliabue, J. S. Duchene, M. Abdellah, A. Habib, D. J. Gosztola, Y. Hattori, W.-H. Cheng, K. Zheng, S. E. Canton, R. Sundararaman, J. Sá, H. A. Atwater, *Nat. Mater.* **2020**, *19*, 1312–1318; f) K. Song, H. Lee, M. Lee, J. Y. Park, *ACS Energy Lett.* **2021**, *6*, 1333–1339; g) R. Li, W.-H. Cheng, M. H. Richter, J. S. DuChene, W. Tian, C. Li, H. A. Atwater, *ACS Energy Lett.* **2021**, *6*, 1849–1856.
[8] H. Kamal, E. K. Elmaghraby, S. A. Ali, K. Abdel-Hady, *J. Cryst. Growth* **2004**, *262*, 424–434.
[9] S. Rakshit, S. Ghosh, S. Chall, S. S. Mati, S. P. Moulik, S. C. Bhattacharya, *RSC Adv.* **2013**, *3*, 19348–19356.
[10] T. Akita, M. Okumura, K. Tanaka, M. Kohyama, S. Tsubota, M. Haruta, *Microscopy* **2005**, *54*, i81–i85.
[11] a) K. Marre, H. Neddermeyer, *Surf. Sci.* **1993**, *287–288*, 995–999; b) K. Koga, M. Hirasawa, *Mater. Res. Exp.* **2014**, *1*, 045021.
[12] Y. Cao, X. Shi, T. Oshikiri, S. Zu, Y. Sunaba, K. Sasaki, H. Misawa, *Chem. Commun.* **2021**, *57*, 524–527.
[13] a) G. Leveque, O. J. Martin, *Opt. Express* **2006**, *14*, 9971–9981; b) H. Sugimoto, S. Yashima, M. Fujii, *ACS Photonics* **2018**, *5*, 3421–3427.
[14] A. Christ, S. G. Tikhodeev, N. A. Gippius, J. Kuhl, H. Giessen, *Phys. Rev. Lett.* **2003**, *91*, 183901.
[15] R. Houdré, J. L. Gibernon, P. Pellandini, R. P. Stanley, U. Oesterle, C. Weisbuch, J. O'Gorman, B. Roycroft, M. Ilegems, *Phys. Rev. B* **1995**, *52*, 7810–7813.
[16] a) Q. Liu, L. Wei, S. Yuan, X. Ren, Y. Zhao, Z. Wang, M. Zhang, L. Shi, D. Li, A. Li, *RSC Adv.* **2015**, *5*, 71778–71784; b) K. Nakamura, T. Oshikiri, K. Ueno, T. Katase, H. Ohta, H. Misawa, *J. Phys. Chem. C* **2018**, *122*, 14064–14071.

Manuscript received: January 28, 2022
Accepted manuscript online: February 20, 2022
Version of record online: March 18, 2022